Front. Mech. Eng. 2022, 17(3): 29
https://doi.org/10.1007/s11465-022-0685-3

RESEARCH ARTICLE

A valveless piezoelectric pump with novel flow path design of function of rectification to improve energy efficiency

Jianhui ZHANG, Xiaosheng CHEN, Zhenlin CHEN, Jietao DAI, Fan ZHANG, Mingdong MA, Yuxuan HUO, Zhenzhen GUI (✉)

School of Mechanical and Electrical Engineering, Guangzhou University, Guangzhou 510006, China

✉ *Corresponding author. E-mail: zhenzhengui@gzhu.edu.cn (Zhenzhen GUI)*

ABSTRACT Existing valveless piezoelectric pumps are mostly based on the flow resistance mechanism to generate unidirectional fluid pumping, resulting in inefficient energy conversion because the majority of mechanical energy is consumed in terms of parasitic loss. In this paper, a novel tube structure composed of a Y-shaped tube and a φ-shaped tube was proposed considering theory of jet inertia and vortex dissipation for the first time to improve energy efficiency. After verifying its feasibility through the flow field simulation, the proposed tubes were integrated into a piezo-driven chamber, and a novel valveless piezoelectric pump with the function of rectification (NVPPFR) was reported. Unlike previous pumps, the reported pump directed the reflux fluid to another flow channel different from the pumping fluid, thus improving pumping efficiency. Then, mathematical modeling was established, including the kinetic analysis of vibrator, flow loss analysis of fluid, and pumping efficiency. Eventually, experiments were designed, and results showed that NVPPFR had the function of rectification and net pumping effect. The maximum flow rate reached 6.89 mL/min, and the pumping efficiency was up to 27%. The development of NVPPFR compensated for the inefficiency of traditional valveless piezoelectric pumps, broadening the application prospect in biomedicine and biology fields.

KEYWORDS composite tube, valveless piezoelectric pump, rectification, energy efficiency

1 Introduction

With the increasing demand for accurate flow control, diversified application scenarios, and complexity of fluid transfer in microchannel, traditional pumps, such as gear pumps and centrifugal pumps [1–5], have difficulty achieving the requirements due to the limitations of their structures and working principles. With the advantages of low energy consumption, compact structure, miniaturization, instant response, precisely controlled energy transfer, and no electromagnetic interference, piezoelectric pumps [6–16] have made remarkable progress as a powerful technique for microfluidic transport, widely used in biomedicine [17–23], thermal management [24,25], precise driving [26–28], and fuel supply [29,30]. Generally, owing to the easier fabrication and simple control strategies, valveless piezoelectric pumps driven by resistance mechanism (VLPPRM) are more attractive in micro-nano applications and have great values in research activities [31–42].

VLPPRMs mainly consist of two parts, pump chamber driven by piezoelectric actuator and valves with no-moving parts. So far, the no-moving parts contain conical tubes [33,36,39], Y-shaped tubes [34,38], spiral tubes [35], vortex diodes [42], and an unsymmetrical chamber with blocks arranged [32]. By designing such structure with a no-moving part, the flow resistances are different when it flows forward and reverse, resulting in different energy losses. Thus, the fluid flow is unidirectional from a net flow standpoint. However, existing VLPPRMs have a common defect of low energy efficiency because the flow channel during suction is the same as that during compression processes. However, the undesirable reflux will happen and impinge the forward pumping fluid, resulting in a majority of the kinetic energy consumed as parasitic loss, which reduces the net flow rate with low pumping efficiency.

To improve the net flow rate, researchers have proposed several solutions mainly focused on two aspects: the structure of vibrator and pump body. To the

Received November 22, 2021; accepted March 14, 2022

former, according to the resonant principle, output amplitude can be amplified by using a resonant vibrator. Park's research group [43–45] first fabricated a resonant piezoelectric pump with high power density, which has a maximum power of 8.7 mW. Later, in Wang's studies, they proposed several resonant piezoelectric pumps, such as folded piezoelectric structure [46] and beam–piezoelectric structure [47]. They all were demonstrated experimentally to realize amplifying output amplitudes and high power density. Mohith's research group proposed a resonant piezoelectric pump with a flexural amplifier and conducted a systematic research on vibration and pumping performance [48–50]. Researchers also proposed other resonant actuators, for example, annular bimorph resonant vibrator [51], U-shaped piezoelectric resonant vibrator [52], and flexible support chamber [53]. The influences of different vibrator modes of resonant piezoelectric actuator on output performance were also explored. The results showed that the first and third bending vibration modes generated simultaneously would bring a higher pumping efficiency than the single-vibrator mode [54].

To improve the structure of the pump body, researchers mainly focus on the design of the no-moving-part valves. Sayar and Farouk [55] investigated the influence of overall pump size on pumping performance, taking a valveless piezoelectric pump with a conical tube as the research object. Ma et al. [56] proposed a piezoelectric pump with rib structures integrated into the chamber, which improved pump efficiency by confining the fluid flowing from inlet to outlet in the shortest path. Zhao et al. [57] proposed a valveless piezoelectric micropump with a crescent-shaped structure to suppress reflux by increasing reflux shock. As the number of crescent-shaped structures increased, the flow rate also increased. To achieve high net flow and low power consumption, Kaçar et al. [58] researched on divergence angle, nozzle/diffuser diameters, lengths, and chamber height. They also obtained the optimized parameters of the pump. Zhang et al. [59] designed a double-outlet valveless piezoelectric pump with a fluid-guiding body. By reducing the return energy of the liquid, the pump's efficiency improved effectively.

To date, the above improved methods for inhibiting backflow are not ideal because the most fundamental problem has not been addressed for which the no-moving-part valves' structure characteristics of dual-wizard pass is always existing. Currently, VLPPRMs remain inefficient. Owing to sharing the same channel, reverse flow resistance changes accordingly when forward flow resistance changes, which greatly limits the freedom of design and application.

In this paper, to improve energy utilization efficiency, the concept of half-wave rectification of electrotechnics into fluid flow is utilized. Based on theory of jet inertia and vortex dissipation, a composite tube (made by a Y-shaped tube and a φ-shaped tube jointing) with the function of rectification is proposed. The fluid from different flow directions flow through dissimilar flow paths. Then, as no-moving part, the composite tubes are integrated into a valveless piezoelectric pump. Herein, a novel valveless piezoelectric pump with the function of rectification (NVPPFR) is realized, which leads the reflux into another path. Therefore, the forward fluid and the reverse fluid are pumped in each flow channel without extra kinetic energy loss by fluid collision, which improves pumping efficiency. Furthermore, mathematical modeling is established, including dynamic analysis of piezoelectric vibrator, fluid dynamics, and efficiency analysis. Finally, various experimental methods, such as the test of amplitude, flow field, flow rate, and pressure, are performed. The designed valveless piezoelectric pump with novel flow path to improve energy efficiency is demonstrated successfully.

2 Structural design

2.1 Design of composite tube

Figures 1(a) and 1(b) show the composite tube with the function of rectification is composed of a Y-shaped tube and a φ-shaped tube jointing. Specifically, the Y-shaped tube is a three-way tube, consisting of two bifurcated tubes and a confluence tube. The two bifurcated tubes are bifurcated by the confluence tube at the angle of 2α and symmetrically distributed with respect to the confluence tube at the same time. The φ-shaped tube is made up of three parts, Channel 1, Channel 2, and a straight tube. Channels 1 and 2 together form a symmetrical annular channel that contains two same semi-arc tubes with the center O/O' and another semi-arc tube with the center O_0. The annular channel is connected to the straight tube to form the tube shaped like the character φ. The two same semi-arc tubes are tangent to another different semi-arc tube and center O, and O' and O_0 locate on a straight line. The straight tube and the confluence tube are on the same line that is tangent to the semi-arc tubes. The diameter of cross-section of the tube is d, the length of the confluence tube is L_1, the length of the straight tube is L_2, the radii of the semi-arc tube are R_1 and R_2, and the bifurcation angle is α.

The designed composite tube achieved the function of rectification for the fluid, which contributed to the result that the fluid from different directions flowed through various flow paths. In Fig. 1(b), the fluid flowed through Channel 1 in direction 1 while flowing through Channel 2 in direction 2. This phenomenon could be explained by jet inertia [60] and vortex dissipation. On the one hand, Figs. 1(c) and 1(d) show that when the fluid flowed through Sections A and B, it mainly flowed along the original direction under the action of inertia. On the other

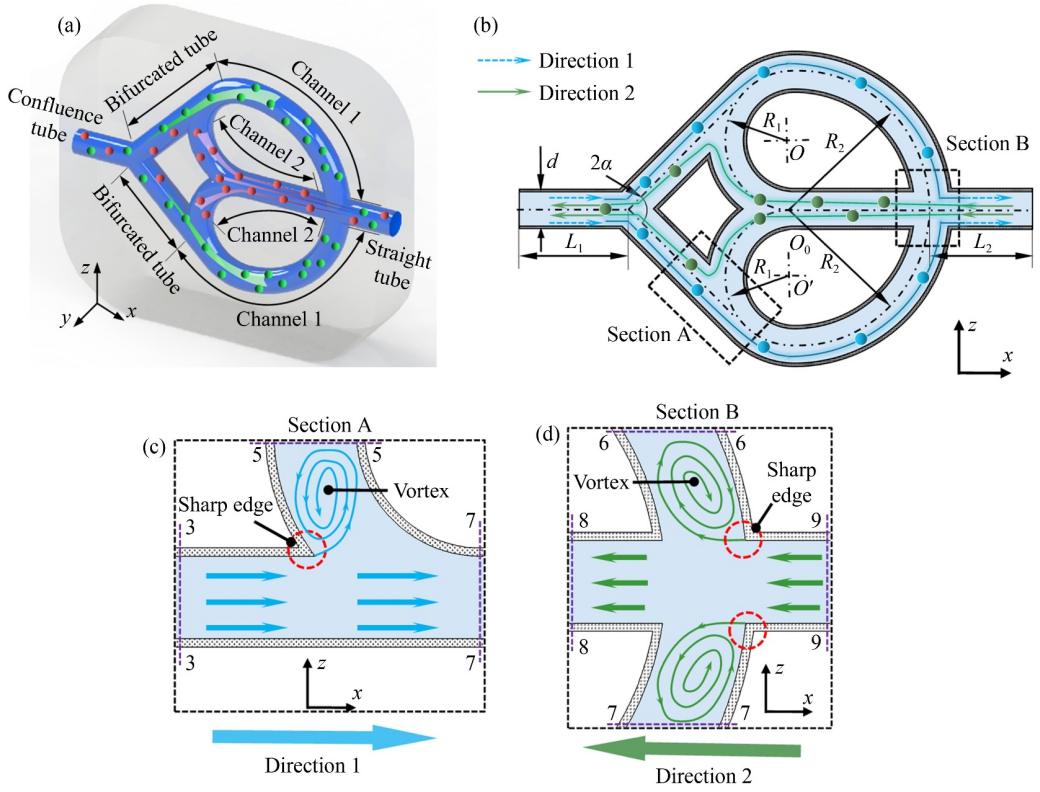

Fig. 1 Structure of composite tube and schematic diagram of rectification. (a) Structure of composite tube, (b) flows of fluid through composite tube in different directions, (c) flows of fluid at Section A, (d) flows of fluid at Section B.

hand, as fluid flowed through the sharp edge of the connection, Helmholtz discontinuity was observed, generating vortices, constantly consuming the kinetic energy of the fluid, and slowing down the flow in consequence.

To verify the feasibility of the proposed composite tube further, the velocity field of the fluid inside composite tube was simulated through computational fluid dynamics. The flow domain of the composite tube was established. The diameter d of the tubes is 2 mm, the length L_1 of confluence tube is 4 mm, the length L_2 of straight tube is 4 mm, and the bifurcation angle α is 45°. The radii R_1 and R_2 are 4 and 8 mm, respectively. Liquid water at room temperature was selected as the working medium, the inlets were set as the boundary pressure of 100 Pa, and the outlets were defined as open boundaries with relative pressure at 0. Non-slip boundaries were defined at wall boundaries. Owing to multiple fluid crossings, the realizable K–ε model was selected for the solution, using a steady-state analysis. Figure 2 presents the simulation results, where the arrow represents the flow direction, successfully verifying the above rectification effect of the composite tube.

The influence of fluid inertia on the rectification effect was also explored by setting different inlet pressures. Velocity fields inside the composite tube under inlet pressures of 100, 200, 300, 400, and 500 Pa were simulated. A dimensionless parameter λ_i, which represents the velocity ratios of fluid between Channels 1 and 2, was defined to compare the rectification effects quantitatively. The pressure loss of the fluid in the tube with a constant cross-section was ignored. Thus, the fluid velocities in Channels 1 and 2 were approximated by the average velocities of the fluid in cross-sections 6–6 and 8–8 in Fig. 2, respectively. Hence, dimensionless parameter λ_i could be written as

$$\lambda_i = \frac{f_{\max}(u_6, u_8)}{f_{\min}(u_6, u_8)}, \tag{1}$$

where $f_{\max}(u_6, u_8)$ and $f_{\min}(u_6, u_8)$ are the maximum and minimum values between u_6 and u_8, respectively.

Figures 3(a) and 3(b) show the average velocity of the fluid in cross-sections 6–6 and 8–8 under the inlets with different pressures. In both directions, the velocity difference of the fluid between cross-sections 6–6 and 8–8 became more apparent with the increase of inlet pressure. Figure 3(c) shows both velocity ratios increased with the increasing pressure, which means the increasing inlet pressure enhanced the function of rectification. Hence, fluid inertia has a great promoting effect on the rectification of fluid inside the composite tube.

2.2 Design of NVPPFR with composite tubes

With the composite tubes as valves, an NVPPFR was achieved. Figures 4(a) and 4(b) show that NVPPFR is

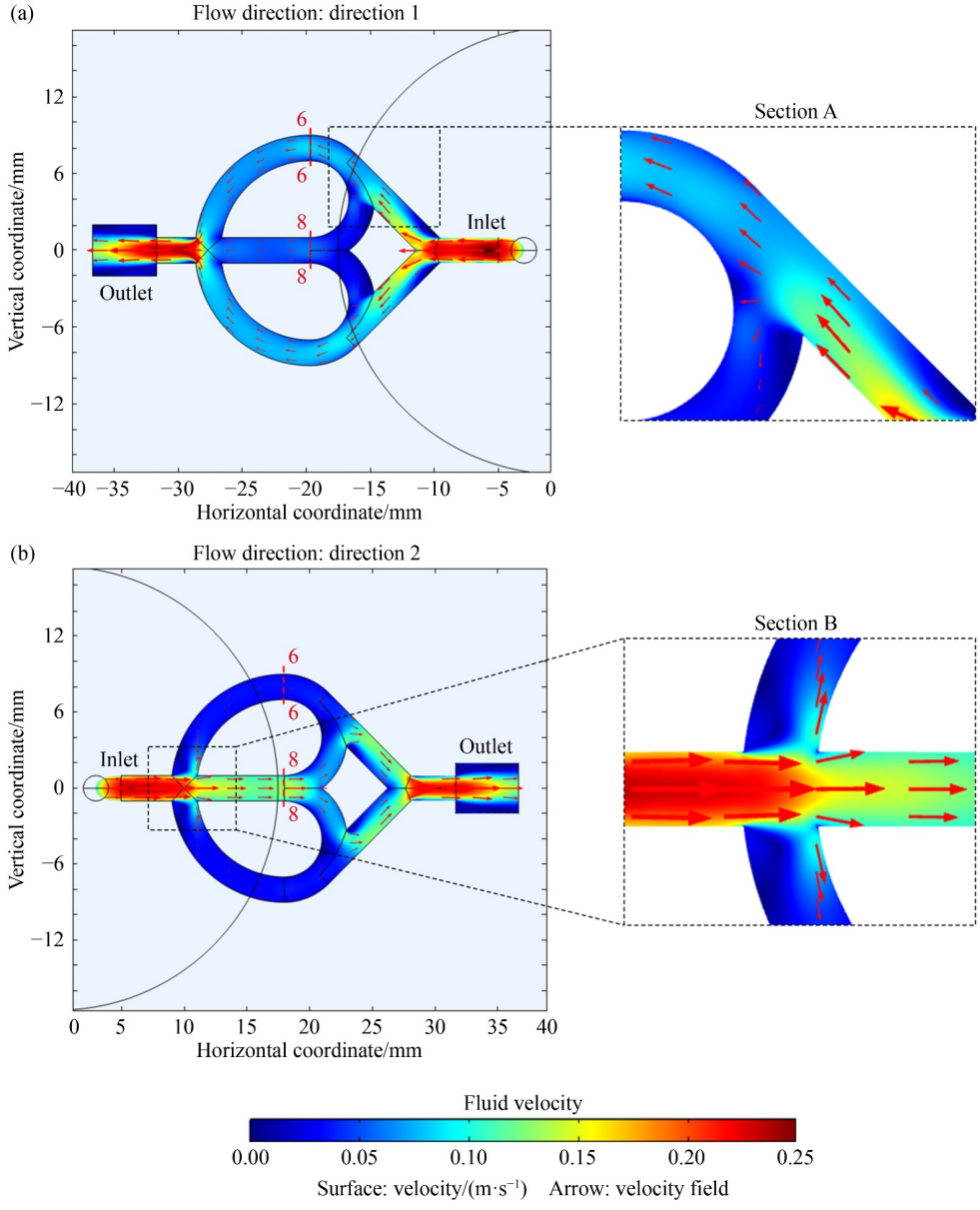

Fig. 2 Simulation results of velocity field on the composite tube in (a) direction 1 on *x*–*y* plane and (b) direction 2 on *x*–*y* plane.

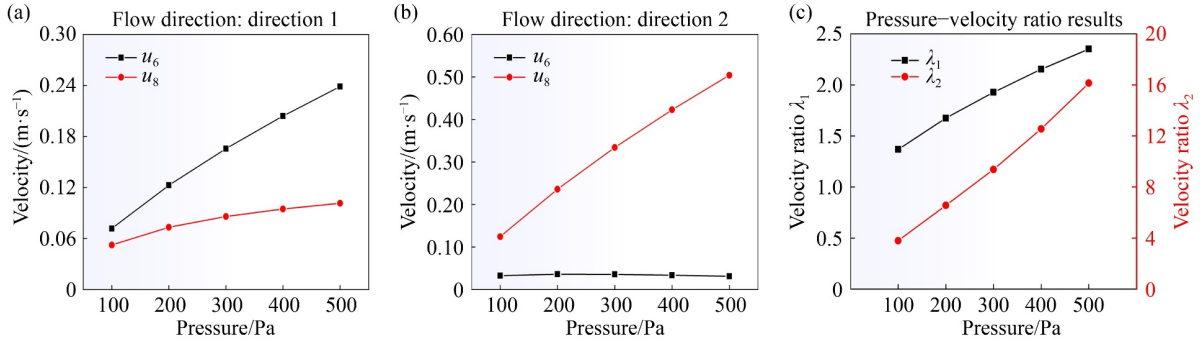

Fig. 3 Simulation results of velocity under inlets with different pressures in directions (a) 1 and (b) 2, velocity of fluid varies with the inlet pressure. (c) Simulation results of velocity ratios vary with pressure.

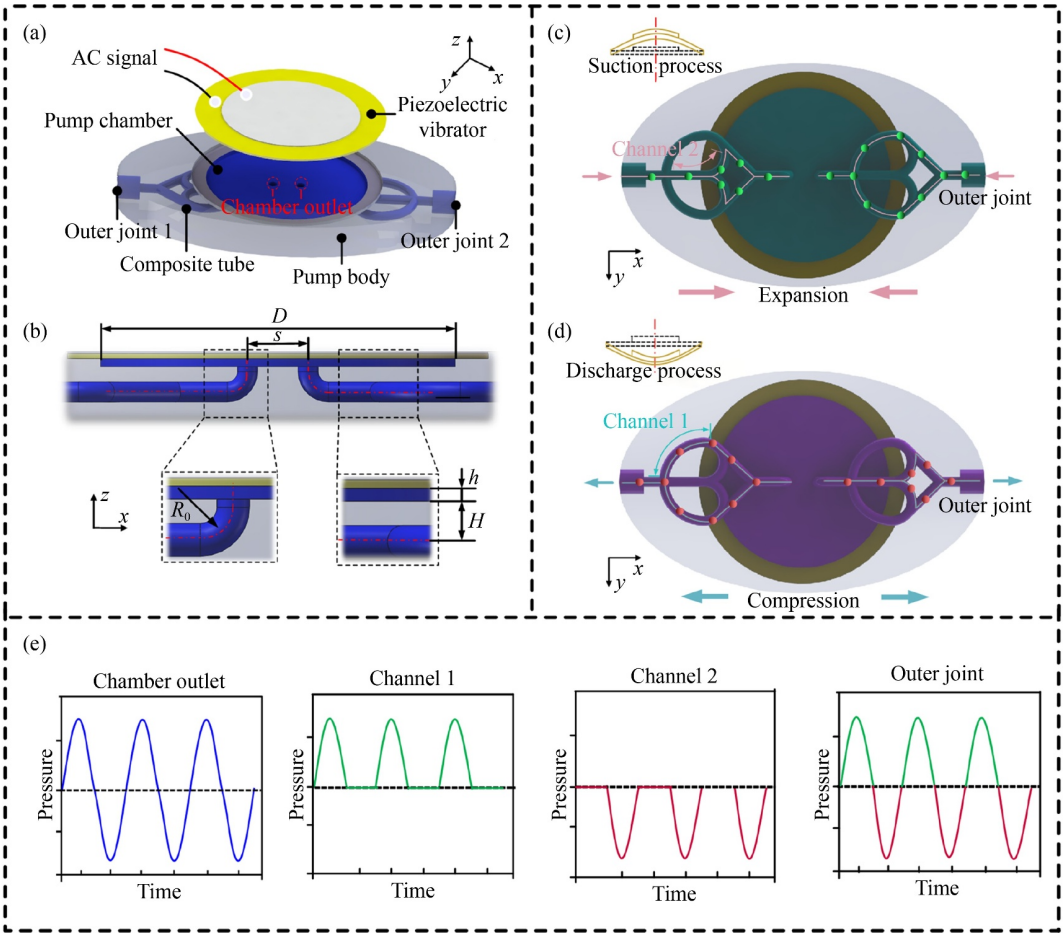

Fig. 4 Structure and working principle of NVPPFR. (a) Structure of NVPPFR, (b) partial view of NVPPFR, (c) flow mechanism during suction, (d) flow mechanism during discharge, (e) calculated fluid pressure at different locations.

composed of piezoelectric vibrator, pump chamber, and pump body. The pump body has two composite tubes connected to the pump chamber as valves. The diameter D_0 of the piezoelectric vibrator is 41 mm, the diameter D of the pump chamber is 35 mm, and the chamber height h is 0.8 mm. The distance s between two chamber outlets is 6 mm, and the radius R_0 of the bend tube connecting the chamber outlets to the composite tubes is 2 mm. The distance H between the composite tubes and the pump chamber is 3 mm.

When a sinusoidal excitation was applied to the piezoelectric vibrator, the conversion of electric energy into mechanical energy occurs under the mechanical–electrical coupling effect. Thus, mechanical stress was generated, forcing the volume of the pump chamber to change periodically. Figures 4(c) and 4(d) show that during suction, the volume of the pump chamber increased with negative pressure occurring, and atmospheric pressure pushed the external fluid through the composite tubes into the pump chamber. During discharge, the volume decreased, and the fluid in the pump chamber was pressed out of the pump chamber through the composite tubes. In a working cycle of "suction–compression" processes, the reverse fluid was led to another channel different from the forward fluid due to the rectification of the composite tubes. Specifically, the external fluid was inhaled into the pump chamber through Channel 1 during suction, whereas the internal fluid was squeezed out through Channel 2 during discharge.

Figure 4(e) shows the pressures of the fluid at different locations. The pressure of the fluid at chamber outlets changed as a sine wave in theory. Through the composite tubes, the fluid was divided into two streams with the pressure change of half sinusoid, which realized the half-wave rectification in fluid flow. The net pressure outputs of Channels 1 and 2 were better than that of the outer joint. Reflux was avoided because the reverse fluid was led to another channel. Hence, the pumping efficiencies in Channels 1 and 2 were greatly improved compared with that in the outer joint. The fluid would be pumped in a unidirectional manner by NVPPFR on a net flow basis due to the differences in kinetic energy loss of fluid between Channels 1 and 2. Therefore, NVPPFRs had rectification effect and pumping effect. Setting Channels 1 and 2 as outlets would obtain a high pumping efficiency.

3 Mathematical modeling

3.1 Dynamic model of piezoelectric vibrator

When the vibration mode of the vibrator is in the first-order mode, the deformation surface is considered a paraboloid. Therefore, the displacement q, velocity $\dot{q}$, and acceleration $\ddot{q}$ of any point on the piezoelectric vibrator are expressed as

$$q = q(r,\theta)\sin(2\pi ft), \tag{2}$$

$$\dot{q} = \frac{\mathrm{d}[q(r,\theta)\sin(2\pi ft)]}{\mathrm{d}t} = 2\pi f q(r,\theta)\cos(2\pi ft), \tag{3}$$

$$\ddot{q} = \frac{\mathrm{d}^2[q(r,\theta)\sin(2\pi ft)]}{\mathrm{d}t^2}, \tag{4}$$

where (r,θ) refers to a location on the piezoelectric vibrator, f is the working frequency of the piezoelectric vibrator, and t is time.

According to Eq. (3), the velocity of the piezoelectric vibrator varies with time. Accordingly, the kinetic energy generated by the piezoelectric vibrator varies over time. In a period, the kinetic energy at the point above the piezoelectric vibrator is expressed as

$$E(r,\theta) = \int_0^{1/(2f)} m(\dot{q})^2 \mathrm{d}t = m\pi^2 f q^2(r,\theta), \tag{5}$$

where $E(r,\theta)$ is the kinetic energy at the point above the piezoelectric vibrator, and m is the mass of the piezoelectric vibrator.

Hence, in unit time, the average kinetic energy per unit mass at the point above the piezoelectric vibrator is expressed as

$$\frac{\partial E(r,\theta) f}{\partial m} = \pi^2 f^2 q^2(r,\theta). \tag{6}$$

The mechanical energy E generated by the deformation of entire surface of piezoelectric vibrator is expressed as

$$E = m\int_0^{2\pi}\mathrm{d}\theta\int_0^R \frac{\partial E(r,\theta) f}{\partial m} r\mathrm{d}r. \tag{7}$$

If the mechanical energy produced by the vibrator completely acts on the fluid of pump chamber, the following relation is obtained:

$$E = E_0 = \frac{1}{2}\rho u_0^2, \tag{8}$$

where E_0 is the initial energy of the fluid, ρ is the density of the fluid, and u_0 is the fluid velocity of the chamber outlet.

3.2 Fluid dynamic model

Fluid resists deformation and produces internal friction to reduce the relative motion of the fluid because the actual fluid is viscous. According to Newton's law of viscosity, the shear stress caused by the relative motion of fluid layers is τ_{ir1} in laminar flow. The turbulent shear stress caused by velocity fluctuation is τ_{ir2} in turbulent flow, which is obtained by Prandtl mixing length theory. Subscript i and r represent flow direction i and flow channel r, respectively. Therefore, the kinetic energy loss of the fluid in the flow channel is regarded as the results of shear stress τ_{ir1} and turbulent shear stress τ_{ir2}. Thus, the following relationships are observed:

$$\boldsymbol{\zeta}_{ir} = \begin{bmatrix} \zeta_{1r}(\tau_{1r1},\tau_{1r2}) \\ \zeta_{2r}(\tau_{2r1},\tau_{2r2}) \end{bmatrix}, \tag{9}$$

$$\begin{bmatrix} \tau_{1r1} \\ \tau_{2r1} \end{bmatrix} = \begin{bmatrix} \mu_{1r}\dfrac{\mathrm{d}u_{1r}}{\mathrm{d}y_{1r}} \\ \mu_{2r}\dfrac{\mathrm{d}u_{2r}}{\mathrm{d}y_{2r}} \end{bmatrix}, \tag{10}$$

$$\begin{bmatrix} \tau_{1r2} \\ \tau_{2r2} \end{bmatrix} = \begin{bmatrix} \mu_{1r}\left(\dfrac{\mathrm{d}u_{1r}}{\mathrm{d}y_{1r}}\right)^2 \\ \mu_{2r}\left(\dfrac{\mathrm{d}u_{2r}}{\mathrm{d}y_{2r}}\right)^2 \end{bmatrix} \begin{bmatrix} l_{1r}^2 & l_{2r}^2 \end{bmatrix}, \tag{11}$$

where $\boldsymbol{\zeta}_{ir}$ is the energy loss coefficient in the direction i inside flow channel r, μ_{ir} is the dynamic coefficient of viscosity, $\dfrac{\mathrm{d}u_{ir}}{\mathrm{d}y_{ir}}$ is the velocity gradient of fluid, and l_{ir} is the Prandtl mixing length. Subscript i represents the direction of fluid flow. When i is 1 and 2, the fluid flows along directions 1 and 2, respectively. Subscript r represents the flow channel. r of 1 and 2 represent the flow channels 1 and 2, respectively.

In Sections A and B, as shown in Figs. 1(c) and 1(d), the cross-sectional area of the fluid expands suddenly, and the fluid flows with the wall constraints of the tube and forms a jet flow without wall constraints. Therefore, based on the flow characteristics of jet flow, the flows of fluid at Sections A and B are deduced. The velocity ratios of fluid in Channels 1 and 2 are expressed as a dimensionless parameter λ_i, and the specific derivation is shown in Appendix. Thus, the kinetic energy $\boldsymbol{E}_{ir}$ of the fluid is expressed as the following matrix:

$$\boldsymbol{E}_{ir} = \begin{bmatrix} E_{11} & E_{12} \\ E_{21} & E_{22} \end{bmatrix} = \begin{bmatrix} \dfrac{\lambda_1^2}{\lambda_1^2+1} & \dfrac{1}{\lambda_1^2+1} \\ \dfrac{1}{\lambda_2^2+1} & \dfrac{\lambda_2^2}{\lambda_2^2+1} \end{bmatrix} E_0. \tag{12}$$

As a result, the fluid kinetic energy loss $\Delta\boldsymbol{E}_{ir}$ is expressed as

$$\Delta\boldsymbol{E}_{ir} = \zeta_{ir}\boldsymbol{E}_{ir}. \tag{13}$$

In addition, due to the different flow rates of fluid between flow channels 1 and 2, mutual pulling force and additional shear stress will be generated during the parallel flow, resulting in extra energy loss $\Delta\boldsymbol{E}_{ie}$. Thus, it can be expressed as

$$\Delta \boldsymbol{E}_{ie} = \boldsymbol{\zeta}_{ie} E_0, \tag{14}$$

where $\boldsymbol{\zeta}_{ie}$ is the extra energy loss coefficient when fluid flowed in the direction i.

In conclusion, based on the analysis of the above, the total energy loss $\Delta \boldsymbol{E}_i$ of fluid flowing in directions 1 and 2 are expressed in matrix form as

$$\Delta \boldsymbol{E}_i = \begin{bmatrix} \Delta E_1 \\ \Delta E_2 \end{bmatrix} = \begin{bmatrix} \zeta_{11} \dfrac{\lambda_1^2}{\lambda_1^2+1} + \zeta_{12} \dfrac{1}{\lambda_1^2+1} + \zeta_{1e} \\ \zeta_{21} \dfrac{1}{\lambda_2^2+1} + \zeta_{22} \dfrac{\lambda_2^2}{\lambda_2^2+1} + \zeta_{2e} \end{bmatrix} E_0. \tag{15}$$

The energy loss coefficient $\boldsymbol{\zeta}_i$ is expressed in matrix form as

$$\boldsymbol{\zeta}_i = \begin{bmatrix} \zeta_1 \\ \zeta_2 \end{bmatrix} = \begin{bmatrix} \zeta_{11} \dfrac{\lambda_1^2}{\lambda_1^2+1} + \zeta_{12} \dfrac{1}{\lambda_1^2+1} + \zeta_{1e} \\ \zeta_{21} \dfrac{1}{\lambda_2^2+1} + \zeta_{22} \dfrac{\lambda_2^2}{\lambda_2^2+1} + \zeta_{2e} \end{bmatrix}. \tag{16}$$

Accordingly, the flow rate Q of pump at outer joint is given by [28]

$$Q = \Delta V f \left| \frac{\zeta_1 - \zeta_2}{2 + \zeta_1 + \zeta_2} \right|, \tag{17}$$

where ΔV represents the volume variation of pump chamber in a half period. If the working fluid is considered incompressible, according to Ref. [13], and ΔV can be expressed as $\Delta V = \pi q R^2$.

3.3 Efficiency analysis

During the work cycle of suction and compression, the kineticenergy loss ΔE of the fluid pumped in a unidirectional manner in the outer joint is expressed as

$$\Delta E = |\Delta E_1 - \Delta E_2| = |(\Delta E_{11} - \Delta E_{21}) - (\Delta E_{12} - \Delta E_{22})|. \tag{18}$$

Pumping efficiency η in the outer joint can be expressed as

$$\eta = \frac{\Delta E}{E_0}. \tag{19}$$

Pumping efficiency η_r in Channels 1 and 2 can be expressed as

$$\eta_1 = \left| \frac{\Delta E_{11} - \Delta E_{21}}{E_0} \right|, \tag{20}$$

$$\eta_2 = \left| \frac{\Delta E_{12} - \Delta E_{22}}{E_0} \right|. \tag{21}$$

4 Experiment design

Stereo lithography apparatus was adopted, and transparent photosensitive resin was used to make the pumps with a molding dimensional accuracy of 0.1 mm. Their parameters are shown in Table 1. The parameters of piezoelectric vibrator used are shown in Table 2.

An experiment was carried out in an indoor environment with no wind interference at a room temperature of 25 °C. The working fluid medium of the sample pump is deionized water with viscosity of 1000 Pa·s.

The function signal generator (AFG1062, Tektronix, USA) was used to provide sinusoidal signal. Then, it was amplified by the power amplifier (HAS4051, NF, Japan) and applied to the piezoelectric vibrator. Performance tests of NVPPFR were carried out, as shown in Fig. 5, mainly including the amplitude test of vibrator, flow rate test, and pressure test of NVPPFR. The oscilloscope (DSO-X2004A, Keysight, USA) was used to monitor the actual applied voltage, current, and frequency of the piezoelectric vibrator. For the amplitude test, the laser displacement sensor (LKH020 (the resolution is 1 μm), Keyence, Japan) was used to measure the amplitudes of the vibrator with the air and deionized water. To obtain the surface deformation of the vibrator, nine equally spaced points were marked, as shown in Fig. 5(b), and the amplitude of each point was measured in the experiments. The flow rate under zero back pressure was tested, as shown in Figure 5(c).

Moreover, Fig. 5(e) shows that to verify the improving pumping efficiency at flow channel 2 further, the forward and reverse pressures at outer joints 3 were tested through dynamic pressure sensor (HM90, HELM, Germany). The range of measurement is between −30 and 30 kPa, accuracy is 0.25%, frequency response is less than 20 kHz, and natural frequency is more than 700 kHz.

Table 1 Structural parameters of piezoelectric pumps

Pump	d/mm	L_1/mm	L_2/mm	R_1/mm	R_2/mm	α/(°)
1	2	4	4	4	8	30
2	2	4	4	4	8	35
3	2	4	4	4	8	40
4	2	4	4	4	8	45

Table 2 Structural parameters of vibrator

Parameters	Values
Resonant frequency	2.1 kHz
Resonant impedance	<175 Ω
Free capacitance	450 nF
Metal plate diameter	41 mm
Metal plate thickness	0.23 mm
Metal plate density	8.5×10^3 kg/m^3
Ceramic disc diameter	36 mm
Ceramic disc thickness	0.30 mm
Ceramic disc density	7.5×10^3 kg/m^3
Total mass	4.3 g

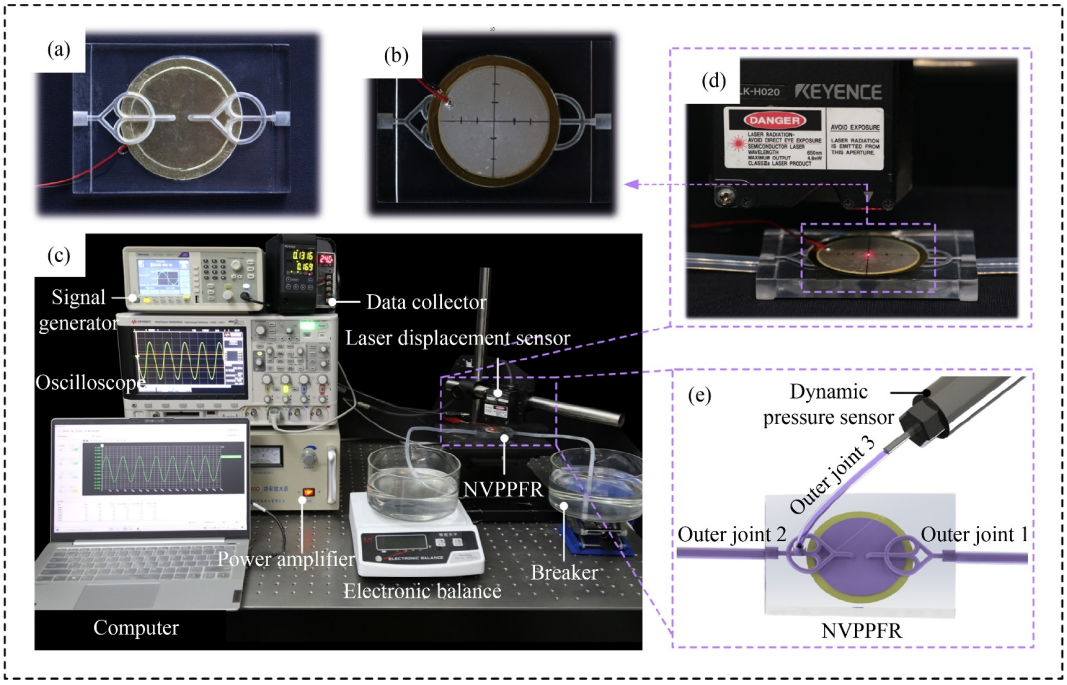

Fig. 5 Performance test of NVPPFR. (a) Bottom and (b) front views of pump; (c) diagram of experimental setups; (d) amplitude test; (e) pressure test.

5 Results and discussion

5.1 Amplitude and kinetic energy of vibrator

Figures 6(a) and 6(b) show the measurement results of the amplitude over the center of vibrators at different pumps and conditions. When deionized water was the working medium, the four groups of pumps showed a good consistency. The amplitudes among them increased at first and then decreased with the change of frequency. PZT (lead zirconate titanate piezoelectric ceramics) pumps 1, 2, 3, and 4 had maximum amplitudes of 49.5 μm at 44 Hz, 60 μm at 44 Hz, 64.5 μm at 38 Hz, and 30.5 μm at 50 Hz, respectively. However, when air was the working medium, the amplitude of the vibrator varied with frequency as a horizontal line. Hence, the type of fluid the pump coupled with had a substantial effect on the mechanical performance of the vibrators. In addition, an approximate linear relationship was noted between amplitude and voltage at the fixed driving frequency of 40 Hz in the range from 50 to 100 V.

According to Eq. (6), the kinetic energy per unit mass of the vibrators at different driving frequencies and voltages could be calculated, as shown in Figs. 6(c) and 6(d). The trends were consistent with the amplitude of the vibrators. PZT pumps 1, 2, 3, and 4 had maximum kinetic energies of 52 mm^2/s^2 at 46 Hz, 70 mm^2/s^2 at 44 Hz, 71 mm^2/s^2 at 42 Hz, and 22 mm^2/s^2 at 50 Hz, respectively. However, the kinetic energy of the vibrator with the working medium of air increased slowly with the increasing frequency.

Moreover, to explore the mode of vibrator, PZT pump 4 was taken as the study sample. Then, the amplitudes of nine equally spaced points at the surface of vibrator were also measured at the driving voltage of 100 V and the driving frequency of 50 Hz in the experiments. Accordingly, the distribution of kinetic energy on the piezoelectric vibrator was obtained, as shown in Fig. 7. The kinetic energy of the vibrator was highest at the center and decayed from the center to the edge. Thus, the variation trends of the kinetic energy along the radial direction were isotropic. Therefore, the vibration of vibrator was roughly regarded in the first-order model.

The above results concluded an evident variance of kinetic energy of vibrator at different driving frequencies under the same driving voltage. Hence, selecting the appropriate driving frequency was vital for a high conversion efficiency. In the operating frequency range of pumps, the mode of vibration was first order, which usually had the ability to generate more kinetic energy. Therefore, the designed pumps had a high energy efficiency.

5.2 Output performances of NVPPFR

When the vibrator had a higher amplitude, the proposed pump had a rectification effect due to the increasing inertia of fluid, resulting in a pumping effect. Figure 8 shows the average pumping flow rate of PZT pump 4 at measurement times of 20, 40, and 60 s. The pumping flow rate at the measurement time of 20 s was the maximum, whereas that at the measurement time of 60 s

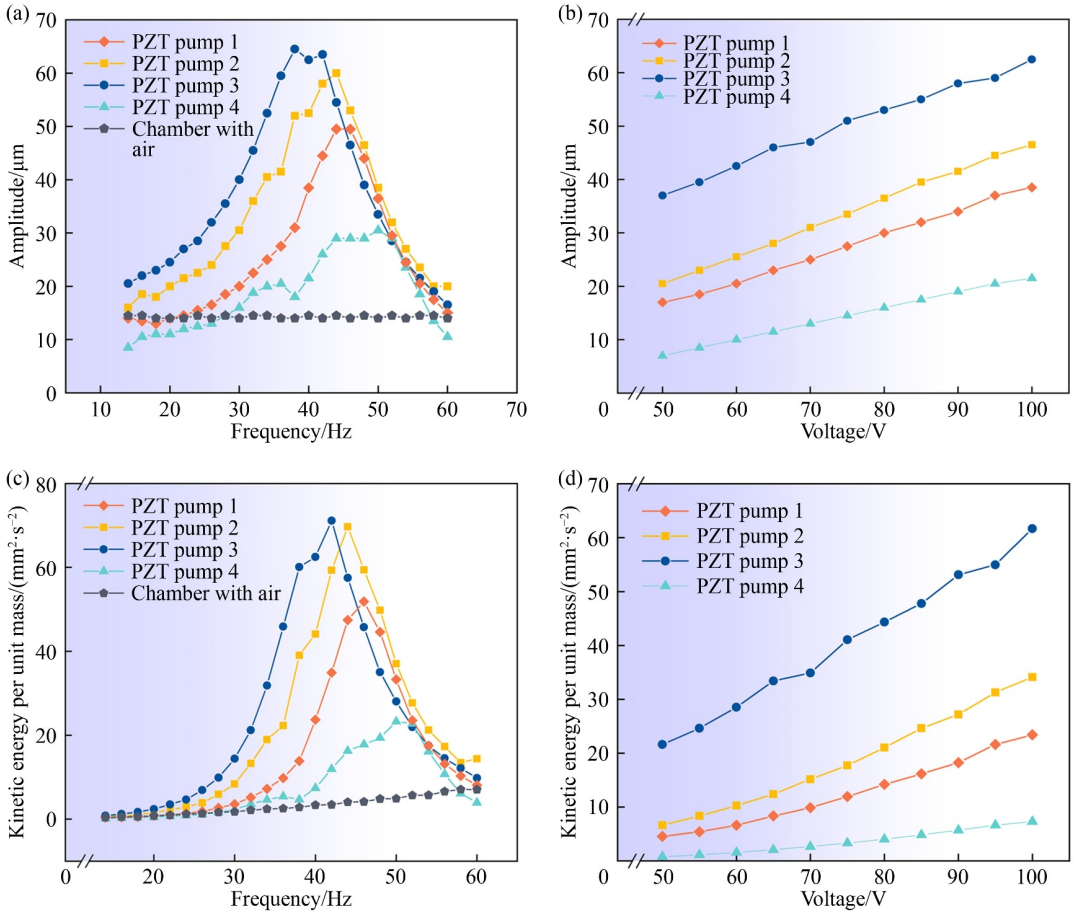

Fig. 6 Amplitude and kinetic energy of vibrators over different pumps. Variation of amplitude with (a) frequency and (b) voltage, and variation of kinetic energy per unit mass with (c) frequency and (d) voltage.

was the minimum because the phenomenon of siphonage appeared and increased pumping resistance as the pumping continued. Therefore, the arithmetic mean of three sets of data measured in different measurement times was selected as the experimental results for the next data analysis. In terms of error, the upper limit of error was the difference between arithmetic mean value and flow rate at 20 s. Similarly, the lower error limit was the difference between arithmetic mean value and flow rate at 60 s.

Hence, the measurement results of net flow rates among the four pumps varied with frequency and voltage, as shown in Fig. 9. The pumping direction of these sample pumps was direction 1, and the trends of flow rate were approximately consistent with the kinetic energy curve of the vibrators. Under a fixed voltage of 100 V, PZT pumps 1, 2, 3, and 4 had maximum net flow rates of 8.02 mL/min at 46 Hz, 12.58 mL/min at 40 Hz, 13.29 mL/min at 38 Hz, and 6.89 mL/min at 44 Hz, respectively. In the range from 50 to 100 V, the flow rate increased with the increasing voltage. The measurement results clearly exhibit that the characteristic of flow rate was consistent with the kinetic energy of the vibrator that was the immediate cause of the pumping flow rate of the pumps. Hence, the output performances of pumps could be adjusted by driving frequency and voltage.

5.3 Pumping efficiency at outer joint and local flow channel

According to previous analysis, the pumping efficiency for the outer joint was obtained by Eq. (19) that is expressed as $\eta = \Delta E / E_0$, and ΔE was obtained by pumping flow rate Q measured in the experiment according to the following relationship:

$$\Delta E = \frac{1}{2}\rho u^2, \tag{22}$$

where u is the sum of velocity vectors of fluid at the outer joint. u can be calculated by $u = Q/S = Q/(\pi r^2)$, where S represents the sectional area of the composite tube.

According to Eq. (8), E_0 was obtained by the amplitude q expressed as

$$E_0 = \frac{1}{2}\rho u_0^2, \tag{23}$$

where u_0 can be calculated by $u_0 = \Delta V f/(2S) = qD^2 f/(8r^2)$.

Thus, the pumping efficiency for the outer joint was expressed as

$$\eta = \frac{u^2}{u_0^2} = \frac{16Q^2}{\pi^2 f^2 q^2 D^4}. \tag{24}$$

In addition, pumping efficiency for Channel 2 was obtained by $\eta_2 = \Delta E_2 / E_0$, and E_2 could be obtained by fluid pressure measured in the experiment. The fluid pressure change in Channel 2 was obtained by experiment. The pressure in compression was defined as forward pressure, whereas that in suction was defined as reverse pressure. At the excitation frequency of 40 Hz and voltage of 120 V, the relationship between fluid pressure and time was a harmonic wave with "noise," as shown in Fig. 10(a). After 1 Hz fast Fourier transformation, the processed curve could be obtained. The variation of forward pressure P_f and reverse pressure P_r with frequency were measured, as shown in Fig. 10(b).

Based on the measuring result of pressure, ΔE_2 and E_0 could be approximated as

$$\Delta E_2 = |P_f - P_r|, \tag{25}$$

$$E_0 = P_f + P_r. \tag{26}$$

Therefore, pumping efficiency η and η_2 for the outer joint and Channel 2 were obtained as well, as shown in Fig. 11. Both efficiencies increased at first and then decreased with the change of frequency. When the efficiencies were at their peaks, their frequencies were approximately the same. Pumping efficiency η for the outer joint had the maximum of 3.64% at 38 Hz, however, efficiency η_2 for Channel 2 had the maximum of 26.41% at 46 Hz, which was nearly seven times as much

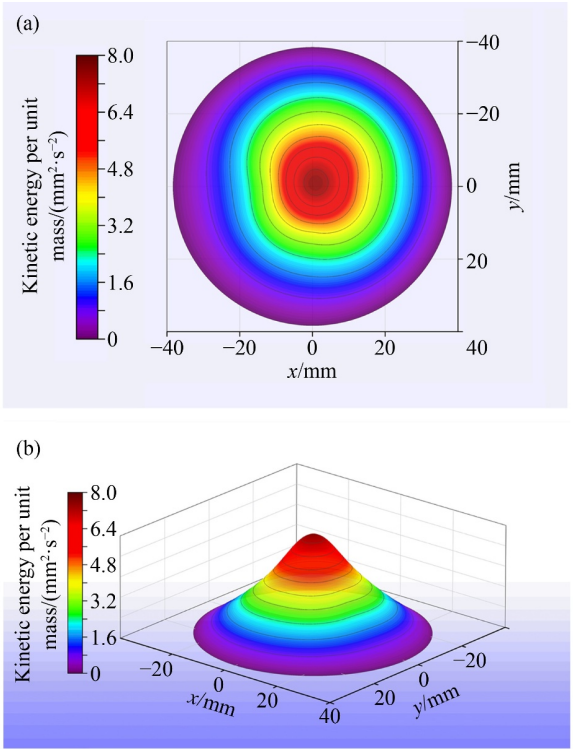

Fig. 7 Distribution of kinetic energy on piezoelectric vibrator. Distribution of kinetic energy on (a) x–y plane and (b) x–y–z space.

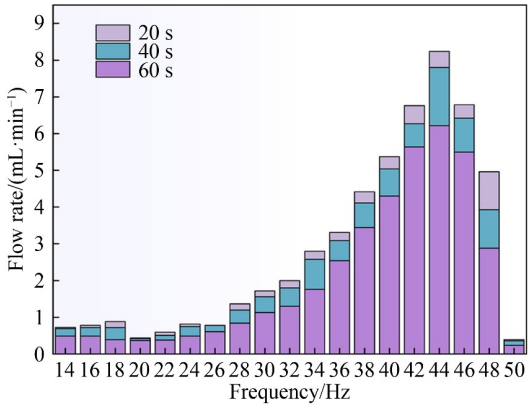

Fig. 8 Flow rate at measurement times of 20, 40, and 60 s.

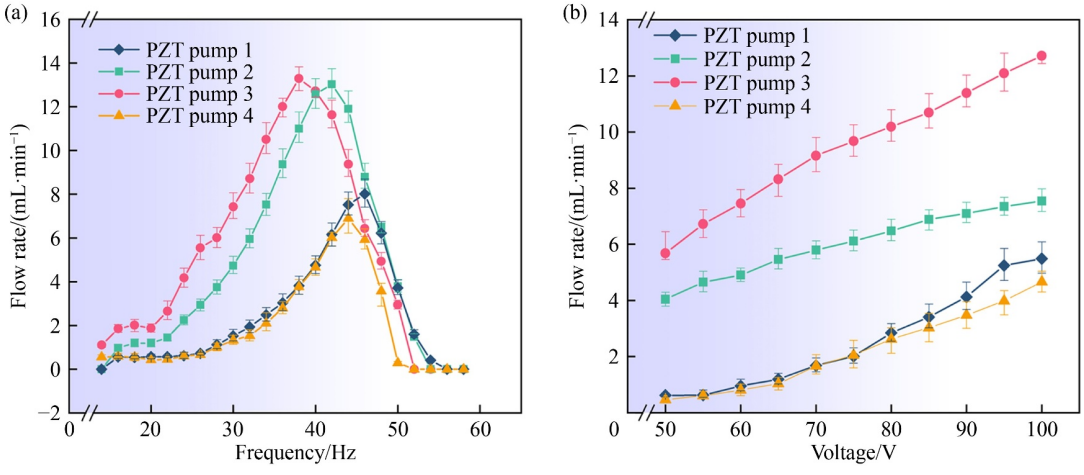

Fig. 9 Net flow rate of different pumps. Variation of net flow rate with (a) frequency and (b) voltage.

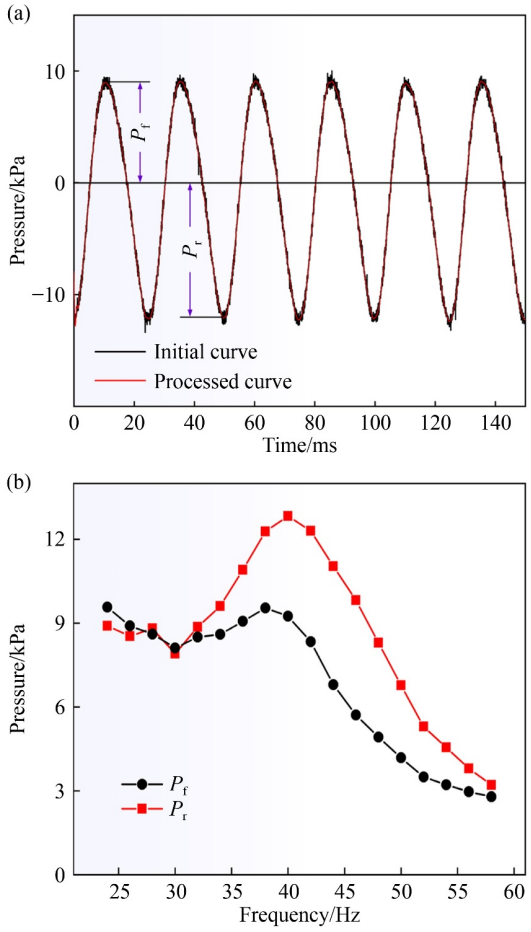

Fig. 10 Pressure change of fluid in Channel 2. Variation of fluid pressure with (a) time and (b) frequency.

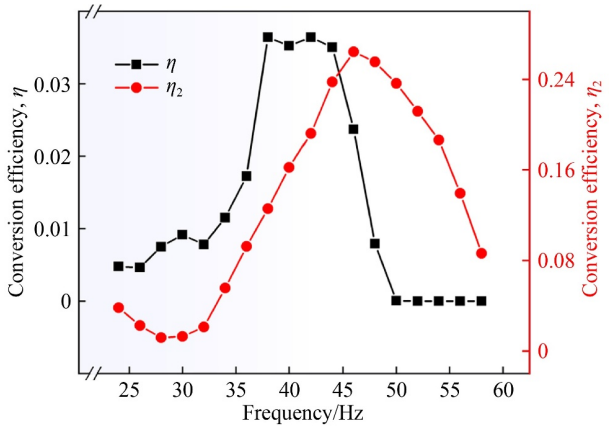

Fig. 11 Calculated results of conversion efficiency for outer joint and Channel 2.

as η. This result verified the feasibility of proposed pump for improving the energy efficiency and indirectly showed that it had the function of rectification.

5.4 Discussion of results

Figure 6 shows a clear variance in the amplitude of the vibrator with different working mediums. When the working medium was air, the amplitude of the vibrator varied with frequency as a horizontal line. However, the amplitude increased first and then decreased with the frequency when deionized water was used. This phenomenon could be explained based on fluid elasticity. The fluid of the pump chamber and the piezoelectric vibrator were considered a unified fluid–solid coupling system. The vibrator acted on the fluid in the pump chamber and generated dynamic pressure of the fluid, which depended on the displacement, velocity, and acceleration of the elastic system vibration. At the same time, the dynamic pressure would change the displacement, velocity, and acceleration in turn. This interaction between vibrator and fluid showed as inertia coupling, damping coupling, and elasticity coupling, which caused the elastic system to produce attachment mass, damping, and stiffness. Therefore, its general equation of motion could be expressed as

$$[M_\varepsilon + M_H]\{\ddot{q}\} + [C_\varepsilon + C_H]\{\dot{q}\} + [K_\varepsilon + K_H]\{q\} = \{F\}, \quad (27)$$

where $[M_\varepsilon + M_H]$, $[C_\varepsilon + C_H]$, and $[K_\varepsilon + K_H]$ are the combined mass matrix, combined damping matrix, and combined stiffness matrix in the unified fluid–solid coupling system, respectively, M_ε, C_ε, and K_ε are the mass, damping, and stiffness of the vibrator, respectively, M_H, C_H, and K_H are the attachment mass, damping, and stiffness causing by fluid coupling, respectively. F is the vector sum of the exciting force.

For the system, resonance frequency f_n was expressed as

$$f_n = \sqrt{\frac{K/M}{2\pi}}, \quad (28)$$

where K is the stiffness of the elastic system, and M is the mass of the elastic system.

The attachment mass M_H and stiffness K_H produced by the elastic system were dissimilar when different kinds of fluids were coupled to the piezoelectric vibrators due to the compressibility difference among various kinds of fluid. Hence, the amplitude and resonance frequency of the piezoelectric vibrator diffed when air and water were used as working medium.

5.5 Comparison with previous fluid diodes

In electronic components, where current is allowed to flow in a single direction only, a device with two electrodes is called an electronic diode. When the current flows forward, the forward resistance is very small, and the current can pass through. However, the reverse resistance is high and the current is blocked when it flows in the opposite direction. Thus, the electronic diodes realize the current of the single wizard, which can change the alternating current into a single direction of pulsating direct current.

In the fluid components, the characteristics of the resistance difference mechanism of the electronic diode are applied to the fluid flow. The tube with difference resistance between positive and negative flow, which is called fluid diode, such as conical tube, Tesla tube, Y-shaped tube, and vortex diodes, is proposed, and its working principle is shown in Fig. 12(a). The positive and negative fluids flow along the same flow channel of the tube. However, the flow resistances of the fluid in different directions through the flow channel are dissimilar. For example, the flow resistance of the fluid along the conical tube is different in the direction of nozzle and diffuser, and the flow resistance along the Y-shaped tube is different in the direction of diversion and confluence. The piezoelectric pumps with fluid diodes can pump the fluid in a unidirectional manner due to difference resistance. This mechanism will unavoidably bring the reflux to impinge the forward pumping fluid, which results in poor efficiency.

Compared with the fluid diode above, the composite tube proposed in this paper has the function of rectification. Figure 12(b) shows that the forward fluid flows through Channel 1, whereas the reverse fluid flows through Channel 2. Thus, the composite tube is called the fluid rectifier diode. The piezoelectric pump with the fluid rectifier diode can correct the reflux fluid to another flow channel different from the pumping fluid. Therefore, in the whole pumping cycle, the forward fluid and the reverse fluid are pumped in each flow channel without extra kinetic energy loss caused by collision of reflux, which improves pumping efficiency. Furthermore, different from traditional fluid diodes, the proposed fluid rectifier diode can realize the advantage that the flow resistance in one direction can be changed separately without affecting the flow resistance in the other direction due to the characteristics of rectification. This setup is unattainable for traditional fluid diode because the reverse flow resistance changes accordingly when the forward flow resistance is changed because they share the same channel. Hence, the proposed fluid rectifier diode greatly increases the freedom of flow channel design for valveless piezoelectric pump, which will benefit designing a piezoelectric pump realizing bidirectional pumping by only controlling driving frequency. It is one of the unsolved issues in the field of piezoelectric pumps and needs to be addressed in our next work.

6 Conclusions

To improve energy efficiency, a composite tube with the function of rectification was proposed based on theory of jet inertia and vortex dissipation. Then, as no-moving part, the composite tubes were integrated into a valveless piezoelectric pump. Thus, an NVPPFR was proposed. Theoretical analysis, simulation, and experiments were conducted to prove its pumping effect, rectification, and high energy efficiency. The following results were obtained:

- NVPPFRs had the pumping effect with the maximum flow rate of 13.29 mL/min.
- The kinetic energy of the vibrator could be adjusted by driving frequencies and voltage, and selecting the appropriate driving frequency was vital for a high conversion efficiency.
- NVPPFR could rectify the reflux fluid to another

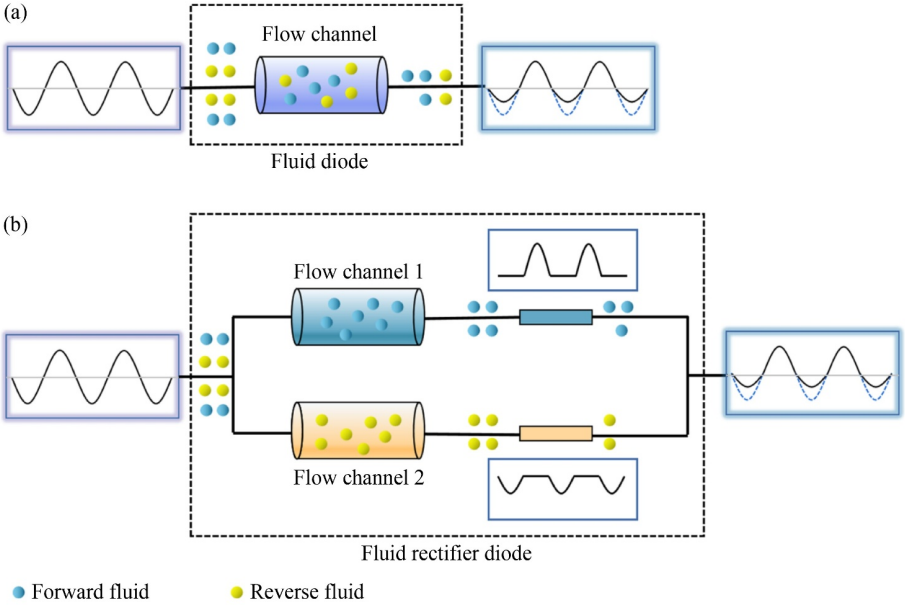

Fig. 12 Comparison between previous fluid diodes and the proposed fluid rectifier diode: working principle of (a) previous fluid diodes and (b) the proposed fluid rectifier diodes.

flow channel different from the pumping fluid, which realized the forward fluid and reverse fluid pumped in each flow channel without extra kinetic energy loss by fluid collision. The pumping efficiency for Channel 2 reached 26.41%, which was nearly seven times as much as that for the outer joint.

- The amplitude and the resonance frequency of the piezoelectric vibrator varied when different working media were used because the attachment mass M_H and stiffness K_H produced by the elastic system were dissimilar when different kinds of fluids were coupled to piezoelectric vibrators.

Appendix

Figure A1 is the simplified hydrodynamic model of fluid flow in the composite tube. In Fig. A1(a), the average velocity u_{13} of the fluid at cross-section 3–3 was regarded as equally distributed velocity when the fluid flowed in direction 1. At Section A, the fluid was considered jet flow, the diffusion angle of jet flow was β, and the thickness of the jet diffused in a linear manner. Thus, the velocity $u_{m'n'}$ of the fluid on the cross-section m′n′ was approximately in the form of Gaussian normal distribution. Therefore, the velocity equation on the cross-section m′n′ could be expressed as

$$u_{m'n'} = u_{1m}\exp\left(-\frac{y_1^2}{b_{half\text{-}1}^2}\right), \tag{A1}$$

where u_{1m} is the maximum velocity of the fluid flowing in direction 1 at cross-section m′n′, and $b_{half\text{-}1}$ is the half characteristic thickness of the jet in direction 1, which is equal to the distance from the place with velocity $u_{m'n'} = u_{1m}/e$ to axis x_1. When jet thickness diffusion coefficient in direction 1 is $\varepsilon_{coef\text{-}1}$ and jet thickness in direction 1 is $b_{thi\text{-}1}$, half-characteristic thickness $b_{half\text{-}1}$ is given by $b_{half\text{-}1} = \varepsilon_{coef\text{-}1} b_{thi\text{-}1}$.

According to the conservation of momentum flux of the jet between sections mn and m′n′, the following relationship could be obtained:

$$\rho u_{13}^2 d = \int_{-\infty}^{+\infty} \rho u_{m'n'}^2 dy_1. \tag{A2}$$

Substituting Eq. (A1) into Eq. (A2), the maximum velocity u_{1m} could be written as

$$u_{1m} = \left(\frac{2d^2}{\pi b_{half\text{-}1}^2}\right)^{\frac{1}{2}} u_{13}. \tag{A3}$$

Therefore, on the x_1–y_1 plane, the flow rates Q_{S15} and Q_{S17} for the flow of the fluid from Section 3–3 to Sections 5–5 and 7–7 are expressed as a matrix for

$$\begin{bmatrix} Q_{S15} \\ Q_{S17} \end{bmatrix} = \begin{bmatrix} \int_{d/2}^{\infty} u_{m'n'} dy_1 \\ \int_{-\infty}^{d/2} u_{m'n'} dy_1 \end{bmatrix}. \tag{A4}$$

When flowing in direction 1, dimensionless parameter λ_1 can be used to express the velocity ratios of fluid in Channels 1 and 2. Thus, the velocity ratios was approximated as

$$\lambda_1 = \frac{Q_{S15}}{Q_{S17}} = \frac{\int_{d/2}^{\infty} u_{m'n'} dy_1}{\int_{-\infty}^{d/2} u_{m'n'} dy_1}. \tag{A5}$$

Given that kinetic energy is a quadratic function of velocity, the relationship of the kinetic energy of fluid in Channels 1 and 2 was expressed as

$$\frac{E_{r11}}{E_{r12}} = \lambda_1^2, \tag{A6}$$

where E_{r11} is the kinetic energy of fluid in Channel 1

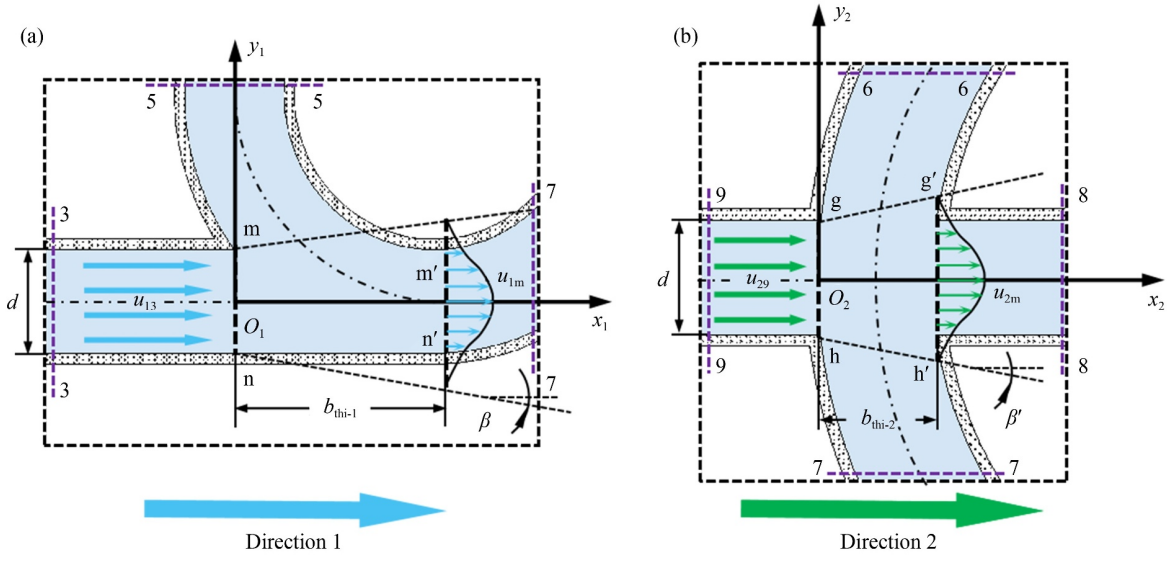

Fig. A1 Model of fluid dynamics in composite tube: fluid dynamics at (a) Section A and (b) Section B.

when fluid flows in direction 1, and E_{r12} is the kinetic energy of fluid in Channel 2 when fluid flows in direction 1.

The fluid dynamics at Section B was also analyzed based on the flow characteristics of the jet. In Fig. A1(b), when the fluid flowed from direction 2, the velocity equation on Section g′h′ was expressed as

$$u_{\mathrm{g'h'}} = u_{2\mathrm{m}} \exp\left(-\frac{y_2^2}{b_{\text{half-2}}^2}\right), \tag{A7}$$

where $u_{2\mathrm{m}}$ is the maximum velocity of the fluid flowing in direction 2 at cross-section g′h′, and $b_{\text{half-2}}$ is the half-characteristic thickness of jet, which is equal to the distance from the place with velocity $u_{\mathrm{g'h'}} = u_{2\mathrm{m}}/\mathrm{e}$ to axis x_2. When thickness diffusion coefficient of the jet is $\varepsilon_{\text{coef-2}}$ and jet thickness is $b_{\text{thi-2}}$, half-characteristic thickness $b_{\text{half-2}}$ is given by $b_{\text{half-2}} = \varepsilon_{\text{coef-2}} b_{\text{thi-2}}$.

Therefore, on the x_2–y_2 plane, flow rates Q_{S26}, Q_{S27}, and Q_{S28} for the flow of the fluid from Section 9–9 to Sections 6–6, 7–7, and 8–8 were expressed as a matrix for

$$\begin{bmatrix} Q_{\mathrm{S26}} \\ Q_{\mathrm{S27}} \\ Q_{\mathrm{S28}} \end{bmatrix} = \begin{bmatrix} \int_{d/2}^{\infty} u_{\mathrm{g'h'}} \mathrm{d}y_2 \\ \int_{-\infty}^{d/2} u_{\mathrm{g'h'}} \mathrm{d}y_2 \\ 2\int_{0}^{d/2} u_{\mathrm{g'h'}} \mathrm{d}y_2 \end{bmatrix}. \tag{A8}$$

When the fluid flowed in direction 2, dimensionless parameter λ_2 can be used to express the velocity ratios of fluid in Channels 1 and 2. Thus, λ_2 can be written as

$$\lambda_2 = \frac{Q_{\mathrm{S28}}}{Q_{\mathrm{S26}} + Q_{\mathrm{S27}}} = \frac{\int_0^{d/2} u_{\mathrm{g'h'}} \mathrm{d}y_2}{\int_{d/2}^{\infty} u_{\mathrm{g'h'}} \mathrm{d}y_2}. \tag{A9}$$

Therefore, the relationship of the kinetic energy of fluid in Channels 1 and 2 was expressed as

$$\frac{E_{r22}}{E_{r21}} = \lambda_2^2, \tag{A10}$$

where E_{r21} is the kinetic energy of fluid in Channel 1 when fluid flowed in direction 2, and E_{r22} is the kinetic energy of fluid in Channel 2 when fluid flowed in direction 2.

According to jet inertia, the larger the flow velocity u of the fluid is, the smaller the diffusion angle of the jet. Thus, the value of dimensionless parameter λ_i satisfies the following relationship:

$$\lim_{u \to \infty} \lambda_i = \infty. \tag{A11}$$

Nomenclature

$b_{\text{half-}i}$	Half characteristic thickness of jet in direction i
$b_{\text{thi-}i}$	Jet thickness in direction i
C_{ε}	Damping of the vibrator
C_{H}	Attachment damping causing by fluid coupling
d	Diameter of cross-section of tube
D	Diameter of pump chamber
D_0	Diameter of piezoelectric vibrator
E	Mechanical energy generated by the deformation of entire surface of piezoelectric vibrator
E_0	Initial kinetic energy of fluid
ΔE	Kinetic energy loss of fluid
$\boldsymbol{E}_{ir}$	Kinetic energy of the fluid
$\Delta \boldsymbol{E}_i$	Total energy loss of fluid flowing
$\Delta \boldsymbol{E}_{i\mathrm{e}}$	Extra kinetic energy loss of fluid
$\Delta \boldsymbol{E}_{ir}$	Kinetic energy loss of fluid
$E(r,\theta)$	Kinetic energy at the point above the piezoelectric vibrator
f	Working frequency of the piezoelectric vibrator
$f_{\max}$	Function that takes the maximum value
$f_{\min}$	Function that takes the minimum value
f_n	Resonance frequency
F	Vector sum of the exciting force
h	Chamber height
H	Distance between composite tubes and pump chamber
K	Stiffness of the elastic system
K_{H}	Attachment stiffness causing by fluid coupling
K_{ε}	Stiffness of the vibrator
L_1	Length of the confluence tube
L_2	Length of the straight tube
l_{ir}	Prandtl mixing length
m	Mass of the piezoelectric vibrator
M	Mass of elastic system
M_{H}	Attachment mass causing by fluid coupling
M_{ε}	Mass of the vibrator
P_{f}, P_{r}	Forward and reverse pressures, respectively
q, $\dot{q}$, $\ddot{q}$	Displacement, velocity, and acceleration of the piezoelectric vibrator, respectively
Q	Flow rate of pump
R_0	Radius of bend tube
R_1, R_2	Radii of the semi-arc tube
s	Distance between chamber outlets
S	Sectional area of the composite tube
t	Time
u	Sum of velocity vectors of fluid at the outer joint
u_0	Fluid velocity of the chamber outlet
$u_{1\mathrm{m}}$	Maximum velocity of the fluid flowing in direction 1 at cross-section m′n′
$u_{\mathrm{m'n'}}$	Velocity of the fluid on the cross-section m′n′
ΔV	Volume variation of pump chamber in a half period
(r,θ)	Polar point
α	Bifurcation angle of tubes
β	Diffusion angle of jet flow
$\varepsilon_{\text{coef-}i}$	Thickness diffusion coefficient in direction i

ρ	Density of the fluid
η	Pumping efficiency in the outer joint
η_r	Pumping efficiency in Channel r
ζ_{ir}	Energy loss coefficient in the direction i inside flow channel r
ζ_{ie}	Extra energy loss coefficient when fluid flowed in the direction i
τ_{ir1}	Shear stress in the direction i
τ_{ir2}	Turbulent shear stress in the direction i
λ_i	Velocity ratios of fluid between Channels 1 and 2
μ_{ir}	Dynamic coefficient of viscosity
$\frac{\mathrm{d}\mu_{ir}}{\mathrm{d}y_{ir}}$	Velocity gradient of fluid
Subscript	
i (i = 1,2)	Flow direction i
r (r = 1,2)	Flow channel r

Credit author statement Jianhui Zhang: methodology, formal analysis, project administration, resources, and funding acquisition. Xiaosheng Chen: formal analysis, validation, investigation, and writing (original draft, review and editing). Zhenlin Chen: software and formal analysis. Jietao Dai: software and visualization. Fan Zhang: writing (review and editing). Mingdong Ma: data curation. Yuxuan Huo: data curation. Zhenzhen Gui: conceptualization, formal analysis, project administration, resources, supervision, and funding acquisition.

Acknowledgements The authors declare that they have no known competing financial interests or personal relationships that could have appeared to influence the work reported in this paper. This work was financially supported by Guangdong Basic and Applied Basic Research Foundation, China (Grant No. 2019B1515120017), Regional Joint Youth Fund Project of Guangdong Basic and Applied Basic Research, China (Grant No. 2020A1515110619), and Guangzhou Science and Technology Plan Project, China (Grant No. 202002030356).

References

1. Castilla R, Gamez-Montero P J, Ertürk N, Vernet A, Coussirat M, Codina E. Numerical simulation of turbulent flow in the suction chamber of a gearpump using deforming mesh and mesh replacement. International Journal of Mechanical Sciences, 2010, 52(10): 1334–1342
2. Arun Shankar V K, Subramaniam U, Paramasivam S, Hanigovszki N. A comprehensive review on energy efficiency enhancement initiatives in centrifugal pumping system. Applied Energy, 2016, 181: 495–513
3. Wang T, Wang C, Kong F Y, Gou Q Q, Yang S S. Theoretical, experimental, and numerical study of special impeller used in turbine mode of centrifugal pump as turbine. Energy, 2017, 130: 473–485
4. Wang Z Y, Qian Z D, Lu J, Wu P F. Effects of flow rate and rotational speed on pressure fluctuations in a double-suction centrifugal pump. Energy, 2019, 170: 212–227
5. Liu H, Zhao B Y, Zhang Z P, Li H B, Hu B, Wang R Z. Experimental validation of an advanced heat pump system with high-efficiency centrifugal compressor. Energy, 2020, 213: 118968
6. Nguyen N T, Huang X Y, Chuan T K. MEMS-micropumps: a review. Journal of Fluids Engineering, 2002, 124(2): 384–392
7. Nguyen N T, Truong T Q. A fully polymeric micropump with piezoelectric actuator. Sensors and Actuators B: Chemical, 2004, 97(1): 137–143
8. Choi S B, Yoo J K, Cho M S, Lee Y S. Position control of a cylinder system using a piezoactuator-driven pump. Mechatronics, 2005, 15(2): 239–249
9. Yakut Ali M, Kuang C F, Khan J, Wang G R. A dynamic piezoelectric micropumping phenomenon. Microfluidics and Nanofluidics, 2010, 9(2–3): 385–396
10. Zhang R H, You F, Lv Z H, He Z C, Wang H W, Huang L. Development and characterization a single-active-chamber piezoelectric membrane pump with multiple passive check valves. Sensors, 2016, 16(12): 2108
11. Zhang J H, Wang Y, Huang J. Advances in valveless piezoelectric pump with cone-shaped tubes. Chinese Journal of Mechanical Engineering, 2017, 30(4): 766–781
12. Ye Y, Chen J, Ren Y J, Feng Z H. Valve improvement for high flow rate piezoelectric pump with PDMS film valves. Sensors and Actuators A: Physical, 2018, 283: 245–253
13. Bao Q B, Zhang J H, Tang M, Huang Z, Lai L Y, Huang J, Wu C Y. A novel PZT pump with built-in compliant structures. Sensors, 2019, 19(6): 1301
14. Peng T J, Guo Q Q, Yang J, Xiao J F, Wang H, Lou Y, Liang X. A high-flow, self-filling piezoelectric pump driven by hybrid connected multiple chambers with umbrella-shaped valves. Sensors and Actuators B: Chemical, 2019, 301: 126961
15. Woo J, Sohn D K, Ko H S. Performance and flow analysis of small piezo pump. Sensors and Actuators A: Physical, 2020, 301: 111766
16. Li H Y, Liu J K, Li K, Liu Y X. A review of recent studies on piezoelectric pumps and their applications. Mechanical Systems and Signal Processing, 2021, 151: 107393
17. Valdovinos J, Williams R J, Levi D S, Carman G P. Evaluating piezoelectric hydraulic pumps as drivers for pulsatile pediatric ventricular assist devices. Journal of Intelligent Material Systems and Structures, 2014, 25(10): 1276–1285
18. Ma H K, Chen R H, Yu N S, Hsu Y H. A miniature circular pump with a piezoelectric bimorph and a disposable chamber for biomedical applications. Sensors and Actuators A: Physical, 2016, 251: 108–118
19. Opekar F, Nesměrák K, Tůma P. Electrokinetic injection of samples into a short electrophoretic capillary controlled by piezoelectric micropumps. Electrophoresis, 2016, 37(4): 595–600
20. Haber J M, Gascoyne P R C, Sokolov K. Rapid real-time recirculating PCR using localized surface plasmon resonance (LSPR) and piezo-electric pumping. Lab on a Chip, 2017, 17(16): 2821–2830
21. Sakuma S, Kasai Y, Hayakawa T, Arai F. On-chip cell sorting by high-speed local-flow control using dual membrane pumps. Lab on a Chip, 2017, 17(16): 2760–2767
22. Wang Y N, Fu L M. Micropumps and biomedical applications—a review. Microelectronic Engineering, 2018, 195: 121–138
23. Chen S, Liu H D, Ji J J, Kan J W, Jiang Y H, Zhang Z H. An

indirect drug delivery device driven by piezoelectric pump. Smart Materials and Structures, 2020, 29(7): 075030
24. Singhal V, Garimella S V, Raman A. Microscale pumping technologies for microchannel cooling systems. Applied Mechanics Reviews, 2004, 57(3): 191–221
25. Tang Y, Jia M Z, Ding X R, Li Z T, Wan Z P, Lin Q H, Fu T. Experimental investigation on thermal management performance of an integrated heat sink with a piezoelectric micropump. Applied Thermal Engineering, 2019, 161: 114053
26. Kaynak M, Ozcelik A, Nama N, Nourhani A, Lammert P E, Crespi V H, Huang T J. Acoustofluidic actuation of *in situ* fabricated microrotors. Lab on a Chip, 2016, 16(18): 3532–3537
27. Wang X R, Jiang H W, Chen Y C, Qiao X, Dong L. Microblower-based microfluidic pump. Sensors and Actuators A: Physical, 2017, 253: 27–34
28. Zhao B, Cui X Y, Ren W, Xu F, Liu M, Ye Z G. A controllable and integrated pump-enabled microfluidic chip and its application in droplets generating. Scientific Reports, 2017, 7(1): 11319
29. Zhang T, Wang Q M. Valveless piezoelectric micropump for fuel delivery in direct methanol fuel cell (DMFC) devices. Journal of Power Sources, 2005, 140(1): 72–80
30. Ma H K, Huang S H, Kuo Y Z. A novel ribbed cathode polar plate design in piezoelectric proton exchange membrane fuel cells. Journal of Power Sources, 2008, 185(2): 1154–1161
31. Dau V T, Dinh T X, Katsuhiko T, Susumu S. A cross-junction channel valveless-micropump with PZT actuation. Microsystem Technologies, 2009, 15(7): 1039–1044
32. Xia Q X, Zhang J H, Lei H, Cheng W. Analysis on flow field of the valveless piezoelectric pump with two inlets and one outlet and a rotating unsymmetrical slopes element. Chinese Journal of Mechanical Engineering, 2012, 25(3): 474–483
33. Tseng L Y, Yang A S, Lee C Y, Cheng C H. Investigation of a piezoelectric valveless micropump with an integrated stainless-steel diffuser/nozzle bulge-piece design. Smart Materials and Structures, 2013, 22(8): 085023
34. Huang J, Zhang J H, Xun X C, Wang S Y. Theory and experimental verification on valveless piezoelectric pump with multistage Y-shape treelike bifurcate tubes. Chinese Journal of Mechanical Engineering, 2013, 26(3): 462–468
35. Leng X F, Zhang J H, Jiang Y, Zhang J Y, Sun X C, Lin X G. Theory and experimental verification of spiral flow tube-type valveless piezoelectric pump with gyroscopic effect. Sensors and Actuators A: Physical, 2013, 195: 1–6
36. Kim C N. Internal pressure characteristics and performance features of the piezoelectric micropumps with the diffuser/nozzle and electromagnetic resistance. Computers & Fluids, 2014, 104: 30–39
37. Wei Y, Torah R, Yang K, Beeby S, Tudor J. A novel fabrication process to realize a valveless micropump on a flexible substrate. Smart Materials and Structures, 2014, 23(2): 025034
38. Huang J, Zhang J H, Shi W D, Wang Y. 3D FEM analyses on flow field characteristics of the valveless piezoelectric pump. Chinese Journal of Mechanical Engineering, 2016, 29(4): 825–831
39. He X H, Zhu J W, Zhang X T, Xu L, Yang S. The analysis of internal transient flow and the performance of valveless piezoelectric micropumps with planar diffuser/nozzles elements. Microsystem Technologies, 2017, 23(1): 23–37
40. Zhang J H, Wang Y, Huang J. Equivalent circuit modeling for a valveless piezoelectric pump. Sensors, 2018, 18(9): 2881
41. Ji J J, Chen S, Xie X Y, Wang X M, Kan J W, Zhang Z H, Li J P. Design and experimental verification on characteristics of valve-less piezoelectric pump effected by valve hole spacing. IEEE Access: Practical Innovations, Open Solutions, 2019, 7: 36259–36265
42. Huang J, Zou L, Tian P, Zhang Q, Wang Y, Zhang J H. A valveless piezoelectric micropump based on projection micro litho stereo exposure technology. IEEE Access: Practical Innovations, Open Solutions, 2019, 7: 77340–77347
43. Park J H, Yoshida K, Yokota S. Resonantly driven piezoelectric micropump: fabrication of a micropump having high power density. Mechatronics, 1999, 9(7): 687–702
44. Park J H, Yoshida K, Nakasu Y, Yokota S, Seto T, Takagi K. A resonantly-driven piezoelectric micropump for microfactory. In: Proceedings of the 6th International Conference on Mechatronics Technology. Tokyo, 2002, 417–422
45. Park J H, Yoshida K, Yokota S, Seto T, Takagi K. Development of micro machines using improved resonantly-driven piezoelectric micropumps. In: Proceedings of the 4th International Symposium on Fluid Power Transmission and Control (ISFP'2003). Wuhan, 2003, 536–541
46. Wang X Y, Ma Y T, Yan G Y, Feng Z H. A compact and high flow-rate piezoelectric micropump with a folded vibrator. Smart Materials and Structures, 2014, 23(11): 115005
47. Wang X Y, Ma Y T, Yan G Y, Huang D, Feng Z H. High flow-rate piezoelectric micropump with two fixed ends polydimethylsiloxane valves and compressible spaces. Sensors and Actuators A: Physical, 2014, 218: 94–104
48. Mohith S, Karanth P N, Kulkarni S M. Performance analysis of valveless micropump with disposable chamber actuated through amplified piezo actuator (APA) for biomedical application. Mechatronics, 2020, 67: 102347
49. Mohith S, Muralidhara R, Karanth P N, Kulkarni S M, Upadhya A R. Development and assessment of large stroke piezo-hydraulic actuator for micro positioning applications. Precision Engineering, 2021, 67: 324–338
50. Mohith S, Karanth P N, Kulkarni S M. Analysis of annularly excited bossed diaphragm for performance enhancement of mechanical micropump. Sensors and Actuators A: Physical, 2022, 335: 113381
51. Wu Y, Liu Y, Liu J F, Wang L, Jiao X Y, Yang Z G. An improved resonantly driven piezoelectric gas pump. Journal of Mechanical Science and Technology, 2013, 27(3): 793–798
52. Chen J, Huang D, Feng Z H. A U-shaped piezoelectric resonator for a compact and high-performance pump system. Smart Materials and Structures, 2015, 24(10): 105009
53. Wang J T, Zhao X L, Chen X F, Yang H R. A piezoelectric resonance pump based on a flexible support. Micromachines, 2019, 10(3): 169
54. Pan Q S, He L G, Huang F S, Wang X Y, Feng Z H. Piezoelectric micropump using dual-frequency drive. Sensors and Actuators A: Physical, 2015, 229: 86–93
55. Sayar E, Farouk B. Dynamic analysis of bulk acoustic wave

piezoelectric micropumps: effects of inlet-outlet port angles and overall pump size. In: Proceedings of the ASME 2013 International Mechanical Engineering Congress and Exposition. Volume 10: Micro- and Nano-Systems Engineering and Packaging. San Diego: ASME, 2013, IMECE2013-66211, V010T11A027

56. Ma H K, Chen R H, Hsu Y H. Development of a piezoelectric-driven miniature pump for biomedical applications. Sensors and Actuators A: Physical, 2015, 234: 23–33
57. Zhao D, He L P, Li W, Huang Y, Cheng G M. Experimental analysis of a valve-less piezoelectric micropump with crescent-shaped structure. Journal of Micromechanics and Microengineering, 2019, 29(10): 105004
58. Kaçar A, Özer M B, Taşcıoğlu Y. A novel artificial pancreas: energy efficient valveless piezoelectric actuated closed-loop insulin pump for T1DM. Applied Sciences, 2020, 10(15): 5294
59. Zhang B C, Huang Y, He L P, Xu Q W, Cheng G M. Research on double-outlet valveless piezoelectric pump with fluid guiding body. Sensors and Actuators A: Physical, 2020, 302: 111785
60. Eggers J, Villermaux E. Physics of liquid jets. Reports on Progress in Physics, 2008, 71(3): 036601